Joule

CellPress

Article

Microscopic Degradation in Formamidinium-Cesium Lead Iodide Perovskite Solar Cells under Operational Stressors

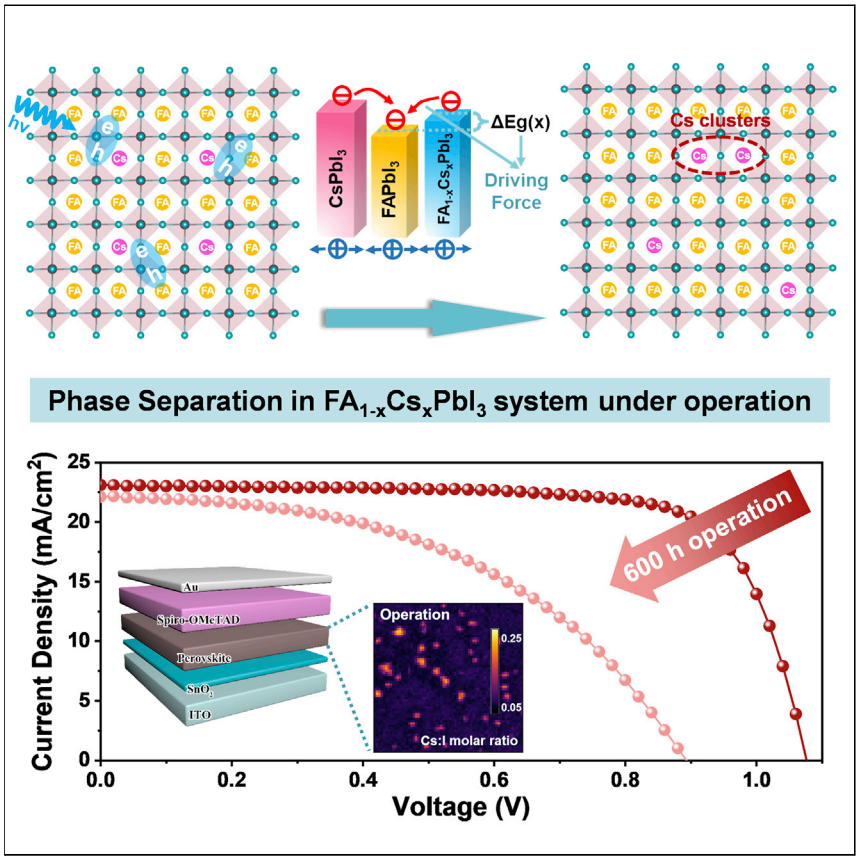

Macroscopic device tests and microscopic material characterization show the segregation of current-blocking Cs-rich phases in $FA_{0.9}Cs_{0.1}PbI_3$ perovskite absorbers under illumination, which is the major reason to cause optoelectronic performance loss in corresponding perovskite solar cells. The underlying degradation mechanism is linked to the light-generated carrier injection level, resulting in a variation in size and density of segregated Cs-rich clusters across stressors.

Nengxu Li, Yanqi Luo, Zehua Chen, ..., Shuxia Tao, David P. Fenning, Huanping Zhou

s.x.tao@tue.nl (S.T.)
dfenning@eng.ucsd.edu (D.P.F.)
happy_zhou@pku.edu.cn (H.Z.)

HIGHLIGHTS

$FA_{0.9}Cs_{0.1}PbI_3$ absorber shows reasonable thermal stability

$FA_{0.9}Cs_{0.1}PbI_3$ absorber is unstable under illumination or operation

Cs-rich phase segregation occurred in $FA_{0.9}Cs_{0.1}PbI_3$ absorbers under illumination

Light-generated carrier injection provides driving force to promote phase segregation

Li et al., Joule 4, 1743–1758
August 19, 2020
https://doi.org/10.1016/j.joule.2020.06.005

Joule

CellPress

Article

Microscopic Degradation in Formamidinium-Cesium Lead Iodide Perovskite Solar Cells under Operational Stressors

Nengxu Li,[1,7] Yanqi Luo,[2,7] Zehua Chen,[3,7] Xiuxiu Niu,[4] Xiao Zhang,[4] Jiuzhou Lu,[4] Rishi Kumar,[2] Junke Jiang,[3] Huifen Liu,[1] Xiao Guo,[1] Barry Lai,[5] Geert Brocks,[3,6] Qi Chen,[4] Shuxia Tao,[3,*] David P. Fenning,[2,*] and Huanping Zhou[1,8,*]

SUMMARY

The most important obstacle to widespread use of perovskite solar cells is their poor stability under operational stressors. Here, we systematically monitor the evolution of the photovoltaic performance of perovskite solar cells based on formamidinium-cesium lead iodide ($FA_{0.9}Cs_{0.1}PbI_3$) for 600 h, under a series of controlled operational stressors. Although these devices exhibit reasonable thermal stability, their stability under illumination or stabilized power output (SPO) is far from commercial demands. Synchrotron-based nanoprobe X-ray fluorescence and X-ray-beam-induced current measurements reveal that current-blocking Cs-rich phases segregate during stress tests. The decrease in performance is in line with the increasing density of the Cs-rich clusters in area upon illumination. Theoretical calculations indicate that light-generated carriers provide the thermodynamic driving force for that phase segregation. Our findings correlate device performance to microscopic behavior and atomistic mechanisms and shed light on inhibiting the cation-dependent phase segregation during device operation.

INTRODUCTION

The performance of organic-inorganic halide perovskite solar cells (PSCs) has improved dramatically in the past decade,[1–8] with the highest certified power conversion efficiency (PCE) of 25.2% using a polycrystalline perovskite absorber,[9] which is approaching state-of-art for crystalline silicon solar cells. However, the poor stability of PSCs in environments of elevated temperature, high humidity, and/or intense irradiation has delayed their commercial deployment.[10–12] Although packaging can extend the stability of PSCs by preventing moisture ingress and reducing evaporation of volatile components in perovskite absorbers upon heating,[13,14] the stability of PSCs under various stressors is still related to many factors, such as the composition and film quality of perovskites, the selection of charge transport layers and electrodes, as well as the device architectures, etc.[12] Particularly, the continuous operation under intense irradiation for PSCs indicates that improving the illumination and operational stability of perovskites[15,16] and understanding the degradation mechanisms accounts for the poor stability remains crucial to the effort to harden PSCs for reliable commercial use.

Halide perovskites are generally in the form of ABX_3, where the A-site contains monovalent cations (i.e., methylammonium [MA^+], formamidinium [FA^+], and Cs^+),

Context & Scale

The instability of perovskite absorbers under various environmental stressors is the greatest obstacle to commercial deployment of corresponding solar cells. Besides degradation, phase segregation is prone to occur in mixed cation perovskites, which deteriorates device performance rapidly and significantly. An improved understanding of the origins of material instability during device operation is expected to provide guidelines for future material design and processing for prolonged device lifetime.

In this study, we investigate formamidinium-cesium lead iodide ($FA_{0.9}Cs_{0.1}PbI_3$) perovskites and corresponding devices under various stressors. While devices exhibit reasonable thermal stability, they show considerable efficiency loss under illumination or operation. The efficiency loss correlates with the occurrence of Cs-rich clusters impacted by stress condition, and the light-generated carriers produce the driving force for this phase segregation.

the B-site contains divalent metal ions (Pb^{2+} or Sn^{2+}), and the X-site contains halides (I^-, Br^-, or Cl^-). For illumination and operation-induced degradation pathways, early works have shown that perovskites present a large amount of Schottky or Frenkel defects,[17,18] which are mainly attributed to the weak bonding in the crystal[19–21] (such as Pb-I ionic bonds, hydrogen bonds, and van der Waals interactions) and the soft crystal lattice.[22] Combined with the low energy barrier for ionic migration,[23,24] halides and organic cations readily migrate through perovskite films, leading to ionic redistribution or even phase segregation upon prolonged testing in the presence of an internal electric field, especially under illumination and/or applied electric load.[25–28] Particularly, phase separation in the hybrid halide (Br and I alloying) system (which can form Br-rich and I-rich phase in perovskites under continuous illumination) have been widely investigated in the $MAPbI_{3-x}Br_x$ perovskites.[28–30] Owing to the obvious band-gap difference between Br-rich and I-rich perovskites (such as 1.59 eV for $MAPbI_3$ and 2.30 eV for $MAPbBr_3$), the detection method on phase separation of Br-I alloying system is commonly dependent on photoluminescence (PL) characterization. This phase separation in mixed halide perovskites potentially originated from the localized strain induced by a single photoexcited charge interacting with the soft and ionic perovskite lattice,[26] and the unfavorable formation energies to induce segregation are overcome by the band-gap reduction of iodide-rich domains.[31] Although there are some studies that demonstrate that based on carbon electrode and triple mesoporous perovskite devices, the incorporation of additives into $MAPbI_3$ can largely extend the illumination lifetime of PSCs (even up to 1 year),[32,33] the thermal instability of MA-containing perovskites is still the Achilles heel to govern the long-term operation of the device.[34]

Recently, the $FA_{1-x}Cs_xPbI_3$ (FACs) system became popular due to its high performance and respectful thermal stability.[35] With the additional constituents, such as Br and Rb, the thermal stability of $FA_{1-x}Cs_xPbI_3$-based PSCs was further improved[36,37] to pass standard 85°C/85% relative humidity (RH) accelerated testing with encapsulation.[38] Meanwhile, they also exhibit considerable stability either under 1-sun illumination[39,40] or in maximum power point (MPP) tracking[36,41] conditions. Although $FA_{1-x}Cs_xPbI_3$-based cells show high thermal stability and gradually increased lifetime under operational conditions, the comprehensive understanding of the stability of these PSCs under various stressors is still lacking. A pioneer study done by Schelhas et al. showed that the degradation pathway of $FA_{1-x}Cs_xPbI_3$ perovskites was associated with phase segregation into the binary phase during operation within 12 h.[42] However, up to now, there was no systematic monitoring of the photovoltaic performance evolution of the $FA_{1-x}Cs_xPbI_3$-based PSCs under various stressors, as well as a microscopic assessment on the magnitude of phase segregation upon different stressors, which is essential for understanding and evaluating the driving forces behind segregation and whether these or similar perovskite materials show promise for durable photovoltaic operation.

In this study, we systematically monitor the performance of high performing MA-free (formamidinium-cesium lead iodide [$FA_{0.9}Cs_{0.1}PbI_3$]) PSCs over 600 h under various environmental conditions, including dark, heat, illumination, and stabilized power output (SPO) (under illumination and fixed electric load). The evolution of the current density-voltage (J-V) as a function of time shows that while $FA_{0.9}Cs_{0.1}PbI_3$-based PSCs exhibit respectable thermal stability, they show considerable performance degradation under illumination and SPO conditions. Materials characterization of the aged perovskite absorbers, using X-ray diffraction (XRD), PL- and synchrotron-based X-ray fluorescence microscopy with nanoscale spatial resolution (nano-XRF), provide evidence for a phase segregation of the original perovskites, where

[1]Beijing Key Laboratory for Theory and Technology of Advanced Battery Materials, Key Laboratory of Polymer Chemistry and Physics of Ministry of Education, BIC-ESAT, Department of Materials Science and Engineering, College of Engineering, Peking University, Beijing 100871, P.R. China

[2]Department of Nanoengineering, University of California, San Diego, La Jolla, CA 92093, USA

[3]Centre for Computational Energy Research, Department of Applied Physics, Eindhoven University of Technology, P.O. Box 513, 5600MB Eindhoven, the Netherlands

[4]Experimental Centre for Advanced Materials, School of Materials Science and Engineering, Beijing Institute of Technology, Beijing 100081, P.R. China

[5]Advanced Photon Source, Argonne National Laboratory, Lemont, IL 60439, USA

[6]Computational Materials Science, Faculty of Science and Technology and MESA+ Institute for Nanotechnology, University of Twente, P.O. Box 217, 7500 AE Enschede, the Netherlands

[7]These authors contributed equally

[8]Lead Contact

*Correspondence: s.x.tao@tue.nl (S.T.), dfenning@eng.ucsd.edu (D.P.F.), happy_zhou@pku.edu.cn (H.Z.)

https://doi.org/10.1016/j.joule.2020.06.005

heterogeneous Cs and FA distributions are identified. Further experiments using *in situ* XRF and X-ray-beam induced current (XBIC) show the Cs-rich clusters to be photoinactive and current blocking, which is likely the main cause of performance loss in $FA_{0.9}Cs_{0.1}PbI_3$ PSCs. First-principles density functional theory (DFT) calculations suggest a thermodynamic driving force for phase segregation, caused by funneling of the photo-generated carriers into FA-rich regions under illumination. Our approach, combining macroscopic device tests, microscopic materials characterization, and atomistic modeling, provides a powerful tool to thoroughly understand the instability of halide perovskites that are intrinsic to device operation, and opens the possibility for designing new perovskite absorber compositions for the ultimate stable PSC.

RESULTS AND DISCUSSION

Device Performance

The PSCs used in this work have the conventional n-i-p architecture: indium tin oxide (ITO)/SnO_2/Perovskite/hole transport layer (HTL)/Au, using the composition of $FA_{0.9}Cs_{0.1}PbI_3$ for the perovskite absorber. More details regarding the device architecture and the fabrication procedure are described in Device Fabrication. The statistics of photovoltaic parameters for the freshly made PSCs (Figure S2; Table S1) show an average PCE of 19.16 $\pm$ 0.55 %, with the champion device achieving a PCE of 20.12% (Figure S3).

To assess PSC instability and underlying failure modes under prolonged stressed testing, we monitored device photovoltaic performance over 600 h of exposure to four distinct stress conditions: 85°C heating in the dark (labeled Heat), 1 sun illumination at near room temperature (35 $\pm$ 10°C) in open-circuit condition (labeled Light), and a SPO at MPP under 1-sun illumination at near room temperature (labeled SPO). The reference sample (labeled Ref) was stored in the dark at room temperature. Notably, all devices were unencapsulated and maintained in an N_2 environment.

Intermittent J-V measurements (Figure 1A) and average cell parameters (Table S2) showed the evolution of the photovoltaic performance of the devices under Ref, Heat, SPO, and Light conditions. Compared with the Ref devices with negligible loss (−1.0%) after 600 h, the Heat, SPO, and Light samples all showed significant losses in PCE (−18.4%, −47.7%, and −66.3%, respectively). Except for the Ref samples, Heat caused the slowest PCE decay due to a slight decrease in fill factor (FF). On the other hand, SPO and Light stressors affected device performance considerably, resulting in significant declines in open-circuit voltage (Voc), short-circuit current (Jsc), and FF (Figure 1A). The stability behavior variation between this study and other recently reported works[36,38,41,43] is likely attributed to the difference in device architecture (n-i-p or p-i-n), absorber composition and film quality (with or without element doping, e.g., Rb or Br), fabrication method (one or two-step solution process) and interface properties (with or without interface passivation layer), etc. Given the competitive stability of Ref samples in this work, and the systematically evaluated performance under various stressors, our result suggests that the $FA_{0.9}Cs_{0.1}PbI_3$ absorber has good thermal stability but can become unstable either under illumination or at the SPO condition.

The photovoltaic performance loss of these devices was further analyzed by tracking the evolution of the J-V curves (Figures 1B–1E). Series resistance (Rs) and shunt resistance (Rsh) were extracted by fitting the J-V curves (Figure S1), and their change as a

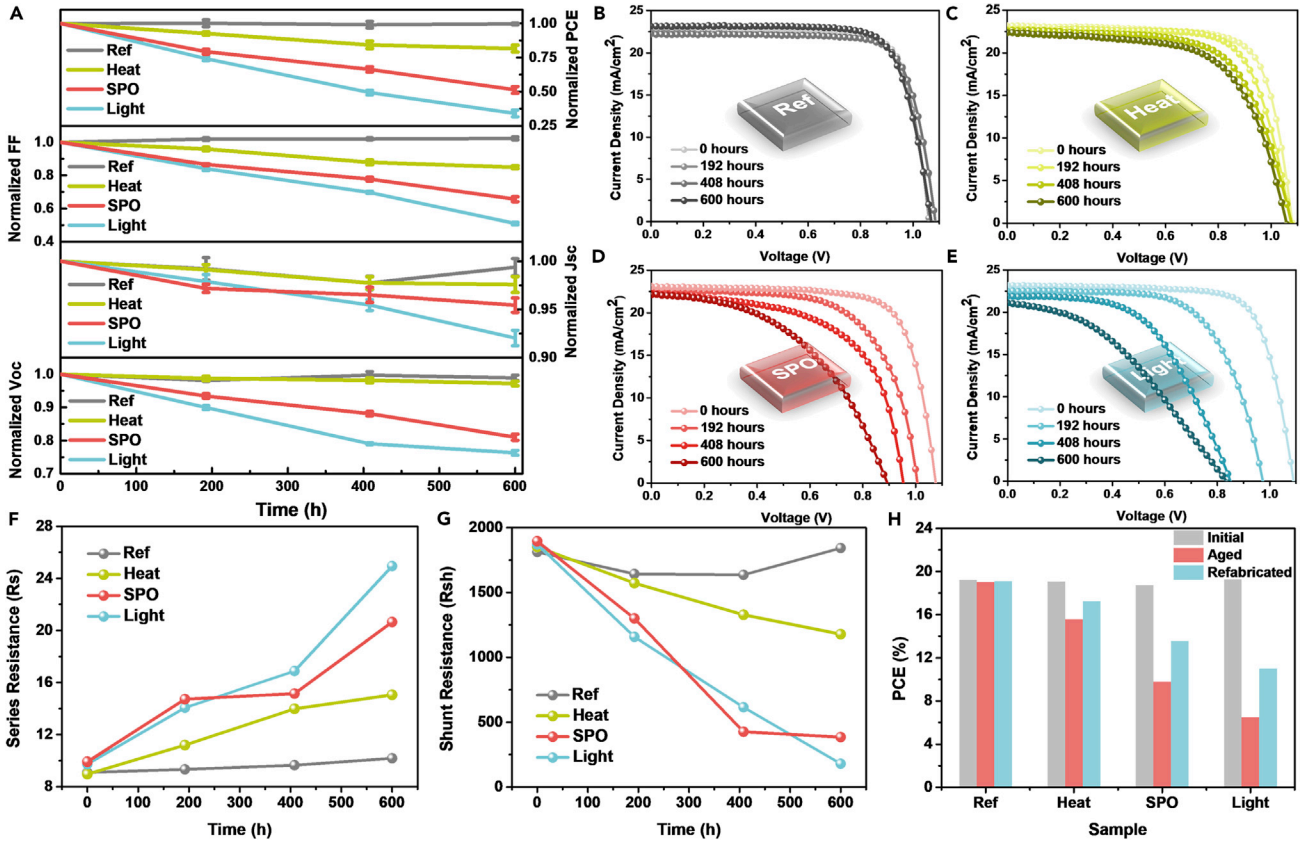

Figure 1. The Evolution of Photovoltaic Performance for Perovskite Solar Cells under Different Environmental Stressors

(A) The evolution of the normalized Voc, Jsc, FF, and PCE of PSCs that aged under different environmental stressors. Eight individual devices were tested for each condition with the mean and the standard deviation shown in the plot.

(B–E) The J-V curves of PSCs after keeping for 0, 192, 408, and 600 h in a nitrogen atmosphere (B) at room temperature under dark (Ref samples); (C) with 85°C heating under dark (Heat samples); (D) SPO tracking under 1 sun illumination at room temperature (SPO samples); and (E) 1 sun illumination at room temperature with open-circuit state (Light samples).

(F and G) The extracted series resistance (Rs) and shunt resistance (Rsh) from light J-V curves (i.e., Figures 1B–1E) are shown in (F) and (G), respectively.

(H) The PCE comparison of initial (no-aged) devices, aged devices, and corresponding refabricated devices under different stressors.

function of stressing time under various stressors is shown in Figures 1F–1G. While Rs increased and Rsh decreased in all stressed devices, which were negative on devices performance, the rate and magnitude of the change of these two parameters was larger in the Light and SPO samples. The decrease in Rsh, indicative of more shunting paths in a solar cell, reduces the value of Voc and FF, as evidenced in Figure 1A. Variations in Rs and Rsh provide information on system level failure of the layer-stacked PSC devices, and further characterization is needed to isolate the impact of environmental stressor on the multiple device layers to help understand decay in performance within these devices.

To exclude the impact of stressing conditions on the Au back-contact and HTL (these two layers are known to degrade under accelerated stressing conditions[44,45]), we re-coated stressed devices with fresh HTL and Au (details are shown in Device Fabrication). Refabricated devices display a significant increase in PCE, compared with that of stressed devices as shown in Figure 1H (details are also shown in Figure S4; Notes S1 and S2), which suggests that stressing conditions indeed have a negative impact on the HTL and Au. Note that the PCE does not recover fully in the refabricated samples that are subjected to Heat, Light, and SPO, indicating that perovskite absorbers

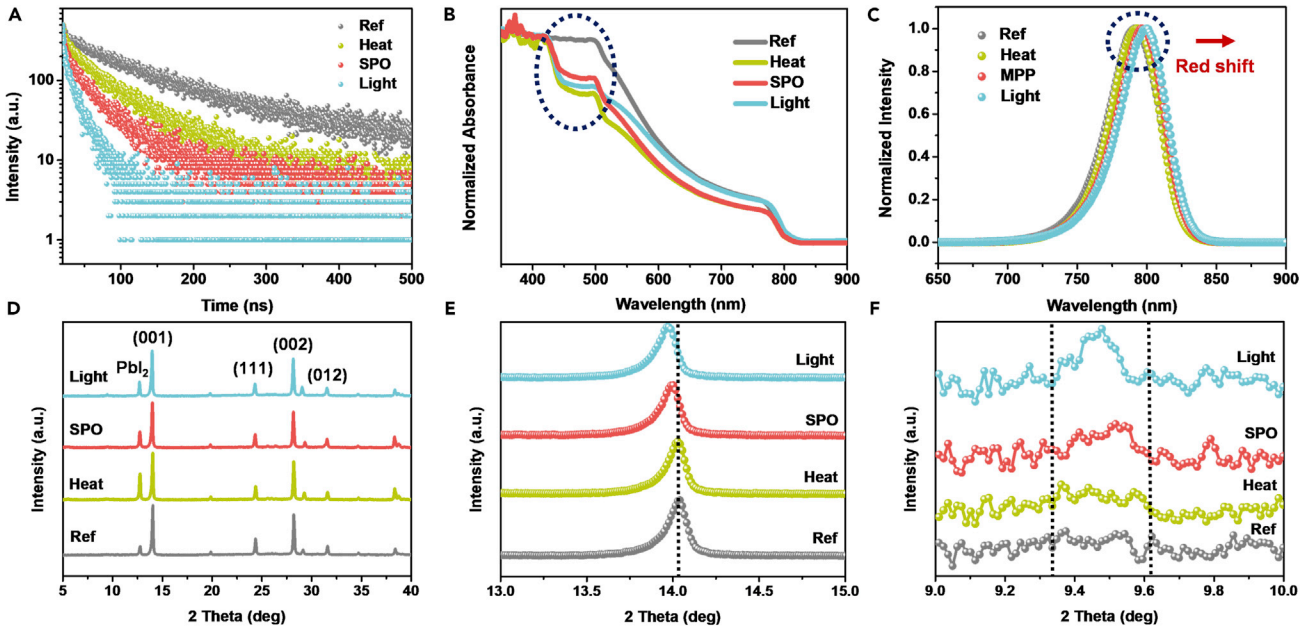

Figure 2. Basic Properties of Perovskite Films Obtained from the Aged Perovskite Solar Cells under Different Environmental Stressors

(A) TRPL decay.

(B) UV-vis spectra.

(C) Normalized steady-state PL spectra.

(D) XRD patterns.

(E) Enlarged XRD patterns from 13° to 15°, the peak around 14° represents the (001) lattice plane of $FA_{0.9}Cs_{0.1}PbI_3$.

(F) Enlarged XRD patterns from 9° to 10°, the peak around 9.5° represents the δ-phase of $CsPbI_3$.

are partially degraded during the aging process and contribute to the remaining performance loss.

In addition, to exclude impact of extrinsic ion migrations, such as Li^+ or Au from the overlaying layers, on degrading absorber performance,[46,47] we prepared half-cells (ITO/SnO_2/perovskite) and stressed them under Heat and Light stressors (half-cells cannot be aged under SPO due to the incomplete device structure), respectively. After 600 h of aging, we fabricated them into whole devices by applying the HTL and Au on top and then measured their photovoltaic performance. There are no obvious performance difference between aged half-cell-based and refabricated devices under light and Heat stressing (Figure S5), indicating that mobile additives within the HTL and Au did not affect the perovskite during the aging. Thus we can conclude that the main source of perovskite degradation after aging is the interaction between environmental stressors and the perovskite itself.

Materials Characterization

To gain insights into perovskite degradation under the different environmental stressors, we characterized the optoelectronic, structural and morphological variations in aged perovskite absorbers (which were obtained by removing the Au electrode and HTL of corresponding PSCs). For comparison, the basic properties of a fresh perovskite film are shown in Figure S6. Time-resolved photoluminescence (TRPL) was used to illustrate carrier lifetime within the stressed samples (Figure 2A and Table S3), where other aged samples have shorter carrier lifetimes than Ref with Light being the shortest followed by the SPO and the Heat. The trend in

carrier lifetime from TRPL is consistent with the corresponding PSCs performance evolution in Figure 1A.

From the UV-vis absorption spectra (Figure 2B), stressed absorbers seem to have a similar absorption to Ref in the wavelength range of 550–850 nm. However, a distinct absorption drop in the range of 450–550 nm is present for all stressed absorbers compared with the Ref sample. We speculate that this absorption loss in aged perovskite films is attributed to the decreased amount of perovskite (which partially decomposed into PbI_2), whereas the PbI_2 itself exhibits much lower molar absorptivity at 500 nm (Figure S7)[48] compared with that of perovskites, as also evidenced by XRD (Figure 2D): the aged Ref sample has the least PbI_2 present and almost no absorption drop, while the Heat sample has higher PbI_2 intensity in the XRD pattern with the largest absorption drop in UV-vis absorption spectra among all the stressed samples. Both UV-vis and XRD measurements suggest that Heat has the largest impact on the formation of PbI_2, confirming heating is indeed a primary cause for the decomposition of the perovskites. However, minor decomposition into PbI_2 may not be detrimental (as shown in Figure 2D). The co-existence of PbI_2 has proven to be effective in passivating defects of perovskites[49,50] and improving the efficiency of PSCs.[51] Thus, we consider that the partial decomposition of perovskite in heat-aged samples has no obvious adverse impact on the optoelectronic performance of corresponding PSCs.

In addition to PbI_2 formation, the (001) perovskite peak shifts to smaller 2θ for Light and SPO samples compared with Ref and Heat films (Figure 2E), indicating an enlarged lattice spacing. This XRD peak shift seems to be associated with a peak shift in PL emission, where red-shifted emission is observed (Figure 2C). These phenomena may be related to a relative enrichment of FA^+ (large cation, compared with Cs^+) on the A-site of Light and SPO perovskites because FA-rich perovskites have larger crystal lattices as well as smaller band gaps. The formation of such FA-rich phase seems to be accompanied by the formation of the δ-phase $CsPbI_3$, evidenced by a new XRD peak found at about 9.5° in the Light and SPO samples (Figure 2F). Both XRD and PL results suggest that the degradation pathway of the $FA_{0.9}Cs_{0.1}PbI_3$ absorber may be a phase transition from the original stoichiometry to an FA-rich perovskite phase ($FA_{>0.9}Cs_{<0.1}PbI_3$) and an FA-poor perovskite phase ($FA_{<0.9}Cs_{>0.1}PbI_3$), even to the formation of $CsPbI_3$ upon Light and SPO stressed conditions. This is further evidenced by PL mapping (Figures 3A–3D), which shows a clear spatial heterogeneity in the Light and SPO compared with the Ref and Heat films. If the PL signals of Ref and Heat samples are considered to originate from $FA_{0.9}Cs_{0.1}PbI_3$, then part of the inhomogeneous PL signals of Light and SPO samples may correspond to FA-rich (yellow regions of PL maps) and FA-poor (brown regions of PL maps) perovskites, respectively.

Furthermore, top view scanning electron microscopy (SEM) images give insight into the micromorphology of aged samples (Figure S8; Note S3). As described above, to exclude the influence of HTL and Au on perovskites under different stressing conditions, the basic properties of aged half-cells (ITO/SnO_2/perovskite) were also characterized (Figure S9 and Table S4). The trend of property evolution in aged half-cells is similar with aged whole devices (details in Note S4), which further exclude the excess effect of HTL and Au on perovskites.

Nano-XRF is used to study, in greater detail, the spatial distribution of the film constituents. Fluorescence maps were collected using a focused synchrotron X-ray probe with a 250 nm full-width half maximum (FWHM). The X-ray energy was set at 7 keV to maximize the measurement sensitivity for I and Cs L-line excitation.

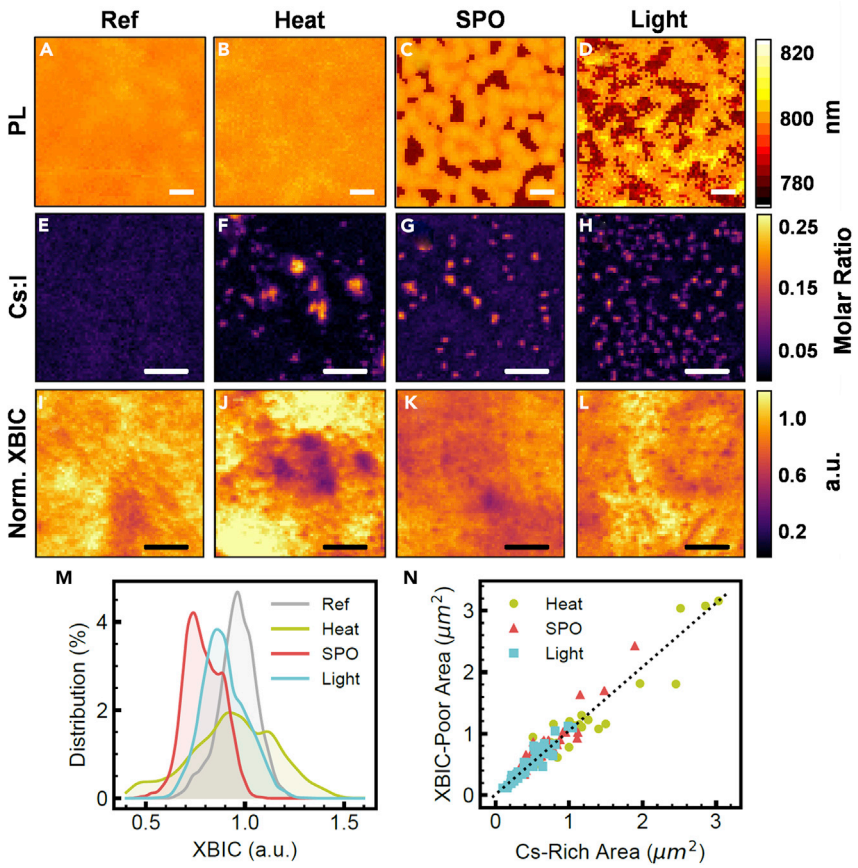

Figure 3. Elemental Distribution of Cs and its Electronic Properties in Perovskites Devices

(A–H) The PL mapping images of perovskite films originated from PSCs (A–D) and X-ray fluorescence (XRF) mapping of perovskite devices (E–H) that are subjected to Ref, Heat, Light, and SPO stressing conditions. The scale bar is 5 μm.

(I–L) X-ray beam induced current (XBIC) mapping of the corresponding regions shown in (E–H). The scale bar is 5 μm.

(M) Pixel-wise frequency distribution of the XBIC observed in each sample.

(N) Correlation of feature areas as measured by XRF (Cs-rich regions) and XBIC (current-poor regions) in Heat, Light, and SPO-treated samples.

The light elements (C, H, and N) in the FA^+ cation were not observable in the XRF measurement.

The local Cs:I stoichiometry is homogeneous within the Ref device, but Cs-rich clusters are observed in all stressed devices (Figures 3F–3H). The number density and size of Cs-rich clusters vary across these three stressors. A few large Cs-rich clusters are seen in the Heat sample, while the clusters become increasingly small and numerous in the SPO and Light conditions. The chemical nature of the Cs aggregates is likely to be a Cs-rich phase (such as $CsPbI_3$, which is detected in Light and SPO samples as shown in Figure 2F) with the highest Cs:I molar ratio of 0.27, which is almost an order of magnitude higher than the ratio in originally prepared perovskite, where the nominal Cs:I molar ratio is expected to be 0.033 for the $FA_{0.9}Cs_{0.1}PbI_3$ stoichiometry.

To reveal the electronic role of these Cs-clusters, XBIC was conducted for Ref and stressed devices simultaneously with XRF measurements. The closed correlation

between local Cs enrichment and reduced current collection indicates that the Cs-rich clusters observed in the Heat, SPO, and Light-treated devices suppress charge collection (Figures 3J–3L). For example, XBIC-poor areas in the centre of Figure 3J are found to align well with the large Cs-rich clusters in the centre of Figure 3F. Similarly, small current suppressing areas in Figure 3K correspond to Cs-rich regions in Figure 3G. The overall effect of the appearance of current suppressing areas is illustrated by histograms of the XBIC signal in each sample shown in Figure 3M. To avoid misinterpretation, the XBIC data shown were corrected to the extent possible for variations in X-ray absorption and subsequent carrier generation due to absorber thickness and morphology variation (Figure S10). This procedure does not remove the effect of morphology fully (e.g., variations remain in the relatively homogeneous Ref sample in Figure 3I), likely due to experimental uncertainty of local film thickness and variation of carrier collection probability with film thickness.

We conclude that the Cs-rich clusters are current-blocking and photoinactive. This was determined by performing a cluster analysis and comparing the feature size of XBIC-poor and Cs-rich areas. A correlation plot of the Cs cluster feature sizes as measured by XRF and XBIC is shown in Figure 3N, in which data from all stressed devices are distributed along the guideline with a slope of 1. The cluster analysis makes explicit the positive correlation and reveals that the XBIC feature size is very close to the size of Cs aggregates in the elemental map.

This microscopic assessment using nano-XRF and XBIC of A-site instability in $FA_{0.9}Cs_{0.1}PbI_3$ devices reveals that the stability of the mixed A-site perovskite phase deteriorated because of thermal and optical energy inputs. Interestingly, a high density of Cs-rich clusters nucleate upon continuous light soaking (light and SPO conditions), while Cs aggregates are larger in size and fewer in number after elevated thermal exposure (85°C). This finer distribution after illumination compared with the Heat sample suggests that there is a smaller critical nucleus size for nucleation of the Cs-rich phase under illuminated conditions. The temperature difference (between the illuminated sample and Heat sample) is not enough to substantially enhance ripening kinetics.[52] On the contrary, illumination is known to enhance ionic conductivity by orders of magnitude.[53] Such enhancements in ion transport would, in principle, facilitate the illuminated sample reaching high density of nuclei relative to the Heat sample within the same stressing time. The Cs-rich particles are smaller and more numerous in the illuminated sample, suggesting that a larger energetic driving force exists for phase segregation under illumination than at 85°C, as in classical nucleation theory the critical radius is inversely related with the thermodynamic driving force.[54]

Mechanism Discussion

The thermodynamic driving force for phase segregation can be identified theoretically, using DFT calculations. We start by computing the mixing enthalpy $\Delta U(x)$ of $FA_{1-x}Cs_xPbI_3$ perovskites as $\Delta U(x)=U_x-(1-x)U_{FA}-xU_{Cs}$, where U_x, U_{FA}, and U_{Cs} are the energies (per formula unit) of $FA_{1-x}Cs_xPbI_3$, the pure $FAPbI_3$ and $CsPbI_3$ perovskites, respectively. An example of a $FA_{1-x}Cs_xPbI_3$ structure used in the DFT calculations is shown in Figure 4A (more details are shown in Table S6). For each composition, we generated a number of structures with FA and Cs cations placed at different random lattice positions. Computational details are given in the DFT Calculations.

The calculated $\Delta U(x)$ curve is shown in Figure 4B. Estimating the entropy contribution by the usual mixing entropy expression $\Delta S(x)=-k_B[x\ln x+(1-x)\ln(1-x)]$

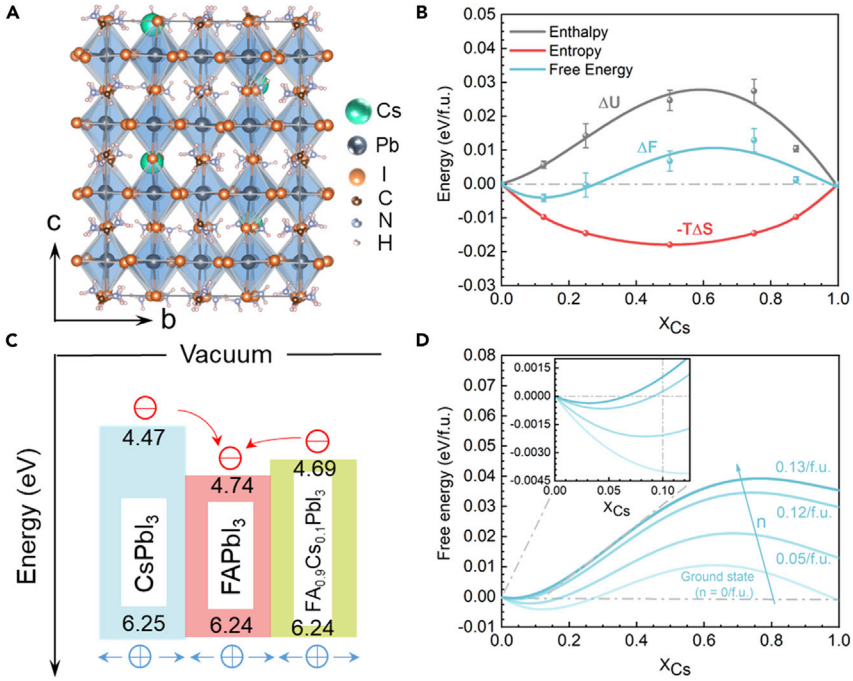

Figure 4. Theoretical Analysis of the Phase Separation Mechanism

(A) Example of a cell of a periodic structure, where 4 out 32 lattice A-sites are occupied by Cs ions, modeling the mixed perovskite $FA_{1-x}Cs_xPbI_3$, with x = 1/8.

(B) Calculated enthalpy (ΔU), the entropy contribution ($-T\Delta S$), and free energy (ΔF) of mixing at room temperature (T = 300 K) under dark conditions, as a function of x. The symbols are the averaged calculated values, the error bars represent the spread found for different random structures, and the solid lines represent polynomial fits.

(C) Band alignment of $CsPbI_3$, $FAPbI_3$, and $FA_{0.9}Cs_{0.1}PbI_3$, the numbers represent the ionization potentials and electron affinities (in eV).[55]

(D) Calculated free energy curves (ΔF^*) as a function of x, at room temperature (T = 300 K), for different photoexcited carrier densities (n). The inset zooms is on the range $0 < x < 1/8$.

allows for calculating the free energy of mixing $\Delta F(x) = \Delta U(x) - T\Delta S(x)$. The $\Delta F(x)$ curve for T=300 K is also shown in Figure 4B. From this figure, it is clearly observed that entropy stabilizes the mixed $FA_{1-x}Cs_xPbI_3$ perovskite for $x \leq 1/4$, with a minimum free energy for a composition x~1/8. This result agrees with our experimental findings that $FA_{0.9}Cs_{0.1}PbI_3$ (x = 0.1) is stable at room temperature and in dark conditions (see the curves marked "Ref" in Figures 1A and 3E; they demonstrate that in the Ref perovskite the Cs ions remain distributed uniformly). Figure 4B also shows that the mixed perovskite becomes unstable for x >1/4, which is consistent with a previous report limiting the amount of Cs that can be incorporated in $FAPbI_3$.[56]

We then modeled the influence of photoexcitation on possible phase segregation in $FA_{1-x}Cs_xPbI_3$ perovskites.[31] Upon illumination, we assume that pairs of charge carriers are generated uniformly in the material at a density (per formula unit) n. This adds a term $nE_g(x)$ to the energy, where $E_g(x)$ is the band gap of the mixed perovskite (for an expression, see Band Gap of $FA_{1-x}Cs_xPbI_3$ Perovskites, Supplemental Information). For the unmixed state: (1−x) $FAPbI_3$ + x $CsPbI_3$, we assume that all charge carriers funnel into the compound with the lowest band gap, which in this case is $FAPbI_3$, see Figure 4C. This adds a term $nE_g^{FA}/(1-x)$ to the total energy of the unmixed state. In summary, under illumination, the mixing energy becomes

$\Delta U^*(x) = n[E_g(x) - E_g^{FA}] + \Delta U(x)$, the last term being the mixing energy under dark conditions, as discussed above.

The mixing free energy $\Delta F^*(x) = \Delta U^*(x) - T\Delta S$, calculated for different values of n, is shown in Figure 4D. Photoexcitation favors phase segregation, essentially because $E_g(x) > E_g^{FA}$ for all compositions $0 < x < 1$, making it always energetically favorable to collect all charge carriers in a pure $FAPbI_3$ compound. Of course, in order to demix $FA_{1-x}Cs_xPbI_3$ into $FAPbI_3$ and $CsPbI_3$, the mixing entropy (Figure 4B) has to be overcome. Figure 4D shows that this happens for n sufficiently large. Over the whole range $0 < x < 1$, we have an increase of the mixing free energy upon illumination. For n sufficiently large, the mixing free energy becomes positive over the whole range, indicating that phase separation is favorable at all Cs concentrations. Similarly, for compositions with a higher concentration of Cs, a larger bandgap difference between the $FA_{1-x}Cs_xPbI_3$ alloys and $FAPbI_3$ is expected, which leads to a higher driving force for phase segregation.

The results of this thermodynamic analysis are consistent with the phase segregation under illumination as observed by XRF elemental mapping (Figures 3G and 3H). The light-treated sample (Figure 3H) shows the largest number density of Cs-rich aggregates. This agrees with the notion that light-generated charge carriers provide a thermodynamic driving force for phase separation. There are fewer Cs-rich aggregates in SPO devices (Figure 3G). We rationalize this by assuming that the average carrier concentration in such devices is lower than that in the light-treated samples, because they are continuously extracted, resulting in a smaller driving force for phase separation.

It should be noted that carrier densities used in these calculations are higher than the typical carrier concentration ($\sim 10^{16}/cm^3$) under 1 sun illumination (see Free Energy upon Photoexcitation, Supplemental Information for details).[57,58] The main reason is that in the simple model explained above we have assumed a uniform carrier density, whereas it is highly likely that even in the mixed perovskite $FA_{1-x}Cs_xPbI_3$, charge carriers funnel into statistically FA-rich regions and are concentrated there, before phase separation starts. That this is indeed the case, is indicated by the redshift of PL peak in Figure 2C. Modeling such a non-uniform carrier density is outside the scope of the present paper.

Our focus on the thermodynamics of $FA_{1-x}Cs_xPbI_3$ does not exclude a role for kinetics. Particularly for samples under long-term light soaking, the ion migration kinetics are faster upon illumination than in dark, due to enhanced ionic conductivity and a reduced migration barrier.[59] The fast ion migration kinetics enhance nucleation rate under illumination.

Unlike the illuminated sample, the origin of secondary phase formation in the Heat-treated sample (85°C) seems to be different. We speculate that the large spots of the Cs-rich phase observed in Figure 3F are the products of a thermally induced decomposition. We note that the calculated decomposition energies (Table S5) of $FAPbI_3$ and $FA_{0.9}Cs_{0.1}PbI_3$ perovskites are markedly smaller than that of the $CsPbI_3$ perovskite.

It should be noted that the most significant performance loss for our FAC PSCs occurred under illumination and operational (SPO) stressors, while the effect of heat on PSC performance (Figure 1A, especially excluding up-layers influence which shown in Figure S4) is comparably small. Generally, it seems that the thermal

decomposition of perovskite absorbers can be largely overcome by composition engineering and device encapsulation. Photodecomposition, however, is considered to be a more challenging issue, not only due to the ionic nature of perovskite absorbers, but also the strong interaction between light and perovskites (such as light induced ionic migration and defect formation). Considering that deployed PSCs must operate under continuous irradiation, a deep understanding of the interaction between perovskites and light is required. Cation-dependent phase segregation in FACs perovskites under illumination is evident in the present work. This provides useful guidance to further modify this system to obtain more efficient and stable PSCs. Possible strategies could include, using functionalized additives to enhance the chemical interaction between ions; doping other elements (such as Br, Rb, etc.) to change the band structure of perovskites; or modifying the energy levels of the charge transport layers to extract photo-carriers more efficiently. Notably, phase segregation is not the sole reason to cause performance loss of FAC-based PSCs, while the cell degradation pathways could be complicated, such as perovskite defects formation, the degradation of other functional layers, bad interface contact, ion migration through whole devices, etc.[12] Even so, our work still provides an effective method to gain insight into determining the relationship between PV performance parameters and absorber degradation at a microscopic level. Most importantly, the combination of optoelectronic performance monitoring, advanced characterization, and theoretical analysis can be expanded to other perovskite systems upon different aging conditions, to deepen the understanding of PSCs, as well as fabricate the optimum PSC.

Conclusion

In summary, we have monitored the evolution of photovoltaic performance in MA-free $FA_{0.9}Cs_{0.1}PbI_3$ PSCs aged over 600 h under stressors intrinsic to PV operation, namely heat, illumination, and SPO. Although $FA_{0.9}Cs_{0.1}PbI_3$-based PSCs exhibit reasonable thermal stability, exposure to 1-Sun illumination induces significant degradation over hundreds of hours of operation. We have established that this degradation correlates with a microscopic phase separation, whereby a Cs-rich phase is formed that is photoinactive and current-blocking. Moreover, we have shown that such a phase separation under illumination is to be expected on the thermodynamic driving force originating from light-generated carriers. Our findings provide a microscopic insight to the performance loss of PSCs under stressors typical for operating conditions, which is vital if designing perovskite materials that are better suited for those conditions.

EXPERIMENTAL PROCEDURES

Resource Availability

Lead Contact

Further information and requests for resources and materials should be directed to and will be fulfilled by the Lead Contact, Huanping Zhou (happy_zhou@pku.edu.cn).

Materials Availability

This study did not generate new unique materials.

Data and Code Availability

This study did not generate or analyze (datasets or code).

Materials

SnO_2 colloid precursor (tin(IV) oxide, 15% in H_2O colloidal dispersion) was purchased from Alfa Aesar. PbI_2 (99.999%), CsI (99.9%), N,N-dimethylformamide

(99.9%), dimethyl sulfoxide (99.5%), isopropanol (99.5%), and chlorobenzene (99.9%) was purchased from Sigma-Aldrich. Spiro-OMeTAD (99.8%) and Poly [bis(4-phenyl)(2,4,6-trimethylphenyl)amine (PTAA) (MOS) was purchased from Xi'an Polymer Light Technology in China. ITO substrate was purchased from Advanced Election Technology Co., Ltd.

Materials Synthesis

FAX (FAI and FACl) were synthesized using the methods reported previously.[16] The details including: 8.8 g formamidine acetate ethanol solution (0.1 mol) was added into a 100 mL three neck flask that was immersed in a water-ice bath. A certain amount (0.12 mol) of HX acid was slowly dropped into the bottle with continuous stirring. The mixture was refluxed for 2 h under N_2 atmosphere. Subsequently, the solution was concentrated to a dry solid by using rotary evaporation at 90°C. This crude product was re-dissolved into 20 mL ethanol, then 100 μL diethyl ether was slowly dropped along the bottle wall, and a white product would deposit. This recrystallization was repeated three times, and the obtained precipitation was dried in a vacuum oven for 24 h at 40°C. The final products were sealed in a N_2-filled glove box for future use.

Device Fabrication

The ITO substrate was cleaned with ultrapure water, acetone, ethanol, and isopropanol, successively. After 30 min of UV-O_3 treatments, a SnO_2 nanocrystal solution (2.5%, diluted by water) was spin coated onto the substrate at 4,000 rpm for 30 s and then annealed at 150°C for 30 min in air. The perovskite film was fabricated by a two-step solution process: the PbI_2 (1.3 M, dissolved in DMF:DMSO [9:1, v:v]) mixed with 10% CsI was spin coated onto ITO/SnO_2 at 2,300 rpm for 30 s and annealed at 70°C for 1 min in a nitrogen glovebox. After cooling the PbI_2-coated substrate to room temperature in a nitrogen glovebox, a mixed organic cation solution (FAI 0.35 M; FACl 0.07M, dissolved in isopropanol) was spin coated with 2,000 rpm for 30 s and then annealed at 150°C for 30 min in air. Then the HTL solution, in which a spiro-OMeTAD/PTAA (36/5 mg mL^{-1}, dissolved in chlorobenzene) mixed solution was employed with the addition of 35 μL Li-TFSI (260 mg mL^{-1}, dissolved in acetonitrile), and 30 μL 4-tertbutylpyridine, was deposited by spin coating at 1,500 rpm for 30 s. The device was finished by thermal evaporation of Au (100 nm) under vacuum.

For refabricated devices mentioned in Figures 1H and S4, before depositing new HTL and Au layers (same processing as previous) on those aged absorbers, we removed the existing Au electrode with adhesive tape and washed off the HTL with chlorobenzene.

Basic Material Characterization

The morphology of perovskite thin films was measured using a cold field-emission SEM equipment (Hitachi S-4800). The XRD patterns were collected using a PANalytical X'Pert Pro X-ray powder diffractometer with Cu Kα radiation (λ = 1.54050 Å). Steady-state PL was measured by FLS980 (Edinburgh Instruments Ltd.) in air (temperature was about 20°C, humidity was about 15% RH) with the excitation wavelength at 470 nm, and we collected the emission signal in the wavelength range from 600 to 900 nm. TRPL was measured by FLS980 (Edinburgh Instruments Ltd.) in air (temperature was about 20°C, humidity was about 15% RH) with the excitation wavelength at 470 nm, to minimize the photo brightening phenomenon.[60] In addition, the TRPL signal collection time for each sample was controlled at about 30 min, so the results were obtained under a relatively stable state. All of these samples are measured under the same process (same excitation wavelength and signal collection

time) and environmental conditions, to ensure the comparability of testing results. PL mapping was measured by a Laser Scanning Confocal Microscope (Enlitech, SPCM-1000) equipped with a 470 nm pulse laser and galvo-based scanner in air (temperature was about 18°C, humidity was about 10% RH). The excitation wavelength was also 470 nm, and we collected the emission signal in the wavelength range from 375 to 1,025 nm. The signal collection area for each sample was 1,225 (35 × 35) μm^2. The UV-vis absorption spectra obtained by an UV-visible diffuse reflectance spectrophotometer (UV-vis DRS, Japan Hitachi UH4150). The J-V characteristics of perovskite devices were obtained using a Keithley 2400 source-measure unit under AM1.5G illumination at 1,000 W/m^2 with a Newport Thermal Oriel 91192 1,000 W solar simulator.

Nano-XRF Characterization

Functional PSCs were investigated by means of synchrotron-based nanoproble X-ray fluorescence (nano-XRF) with a 250 nm FWHM-focused beam at 7 keV at beamline 2-IDD in a helium environment of the Advanced Photon Source (APS) at Argonne National Laboratory. The nano-XRF measurement was conducted with the backside Au contact facing the incident X-ray beam, with a full fluorescence spectrum collected point by point during mapping. MAPS software was used to fit and deconvolute overlapping peaks and background removal from the fluorescence data.[61] Cs and I XRF signals were quantified using XRF standards purchased from MICROMATTER Tech Inc. Au and Pb signals were quantified using NIST-1832/1833.

In Situ nano-XRF and XBIC Characterization

The *in situ* nano-XRF and XBIC characterization was conducted using a similar setup as previous studies,[62] where the focused X-ray beam penetrates through the backside Au contact, allowing collection of both elemental distribution (nano-XRF) and XBIC simultaneously, with 250 nm step size and a dwell time per point of 50 ms. A lock-in amplifier (Stanford Research SR380) and a current pre-amplifier (Stanford Research SR570) at the beamline were used together to collect the induced current signal for XBIC. To acquire a higher signal-to-noise elemental XRF map, a second "elemental" map was collected using a step size as small as 150 nm (oversampling) with dwell time per point of 150 ms.

Density Functional Theory Calculation

To model the mixed-A-cation perovskites, $FA_{1-x}Cs_xPbI_3$, we started from a periodic tetragonal supercell containing 32 formula units of $FAPbI_3$ with an initially randomized orientation of FA cations.[63] We then replaced FA cations by Cs cations at different concentrations (x = 0, 1/8, 1/4, 1/2, 3/4, 7/8, and 1). We considered three possible configurations of Cs ions at each concentration. An example of a structure is given in Figure 4A of the main text.

All the calculations were performed using the DFT approach. We used the projected augmented wave (PAW) method and the Perdew, Burke and Ernzerhof (PBE) exchange-correlation functional within the generalized gradient approach (GGA)[64,65] functional, as implemented in the Vienna *ab initio* simulation package (VASP).[66] The plane-wave cutoff energy is set at 500 eV, and the Brillouin zone was sampled with the Γ point only. An accuracy of 0.01 meV was adopted for the electronic loops. The shape and volume of the supercell, as well as the atomic positions of each configuration were fully optimized. The convergence criteria on total energy and forces are set at 0.01 meV and 0.02 eV/Å, respectively.

SUPPLEMENTAL INFORMATION

Supplemental Information can be found online at https://doi.org/10.1016/j.joule.2020.06.005.

ACKNOWLEDGMENTS

This work was supported by National Natural Science Foundation of China (grant nos. 51722201, 51672008, 51972004, and 91733301); National Key Research and Development Program of China grant no. 2017YFA0206701; Natural Science Foundation of Beijing, China (grant no. 4182026). The work at UC, San Diego was supported in part by the California Energy Commission (EPC-16-050) and the National Science Foundation under grant no. DMR-1848371. The work at Eindhoven University of Technology was supported by the Computational Sciences for Energy Research (CSER) tenure track program of Shell and NWO, the Netherlands (project number 15CST04-2).

AUTHOR CONTRIBUTIONS

H.Z. and N.L. conceived the idea and designed the experiments; D.P.F., Y.L., and R.K. were involved in experiment discussion and performed *in situ* nano-XRF and XBIC measurements; S.T. and G.B. designed and Z.C. and J.J. performed the DFT calculations; N.L., X.N., X.Z., C.Z., J.L., C.W., X.G., and H.L. contributed to the fabrication of PSCs; N.L. and X.N. performed UV-vis, XRD, PL, SEM, and PL mapping characterizations; B.L. provided beamline support at 2IDD APS for XRF and XBIC measurement; H.Z., D.P.F., S.T., N.L., Y.L., and Z.C. wrote the manuscript; X.N., Q.C., R.K., and G.B. revised the manuscript. All authors were involved in the discussion of data analysis and commented on the manuscript. N.L., Y.L., and Z.C. have contributed equally to this work.

DECLARATION OF INTERESTS

The authors declare no competing interests.

Received: February 12, 2020
Revised: April 21, 2020
Accepted: June 3, 2020
Published: July 10, 2020

REFERENCES

1. Kojima, A., Teshima, K., Shirai, Y., and Miyasaka, T. (2009). Organometal halide perovskites as visible-light sensitizers for photovoltaic cells. J. Am. Chem. Soc. *131*, 6050–6051.

2. Kim, H.S., Lee, C.R., Im, J.H., Lee, K.B., Moehl, T., Marchioro, A., Moon, S.J., Humphry-Baker, R.H., Yum, J.H., Moser, J.E., et al. (2012). Lead iodide perovskite sensitized all-solid-state submicron thin film mesoscopic solar cell with efficiency exceeding 9%. Sci. Rep. *2*, 591.

3. Snaith, H.J. (2013). Perovskites: the emergence of a new era for low-cost, high-efficiency solar cells. J. Phys. Chem. Lett. *4*, 3623–3630.

4. Zhou, H., Chen, Q., Li, G., Luo, S., Song, T.B., Duan, H.S., Hong, Z., You, J., Liu, Y., and Yang, Y. (2014). Photovoltaics. Interface engineering of highly efficient perovskite solar cells. Science *345*, 542–546.

5. Yang, W.S., Noh, J.H., Jeon, N.J., Kim, Y.C., Ryu, S., Seo, J., and Seok, S.I. (2015). Solar cells. High-performance photovoltaic perovskite layers fabricated through intramolecular exchange. Science *348*, 1234–1237.

6. Yang, W.S., Park, B.W., Jung, E.H., Jeon, N.J., Kim, Y.C., Lee, D.U., Shin, S.S., Seo, J., Kim, E.K., Noh, J.H., and Seok, S.I.L. (2017). Iodide management in formamidinium-lead-halide–based perovskite layers for efficient solar cells. Science *356*, 1376–1379.

7. Jiang, Q., Zhao, Y., Zhang, X., Yang, X., Chen, Y., Chu, Z., Ye, Q., Li, X., Yin, Z., and You, J. (2019). Surface passivation of perovskite film for efficient solar cells. Nat. Photonics *13*, 460–466.

8. Min, H., Kim, M., Lee, S.U., Kim, H., Kim, G., Choi, K., Lee, J.H., and Seok, S.I. (2019). Efficient, stable solar cells by using inherent bandgap of α-phase formamidinium lead iodide. Science *366*, 749–753.

9. NREL National Center for Photovoltaics (2019). Best research-cell efficiency chart. https://www.nrel.gov/pv/cell-efficiency.html.

10. Leijtens, T., Eperon, G.E., Noel, N.K., Habisreutinger, S.N., Petrozza, A., and Snaith, H.J. (2015). Stability of metal halide perovskite solar cells. Adv. Energy Mater. *5*, 1500963.

11. Berhe, T.A., Su, W.N., Chen, C.-H., Pan, C.-J., Cheng, J.-H., Chen, H.-M., Tsai, M.-C., Chen, L.-Y., Dubale, A.A., and Hwang, B.-J. (2016). Organometal halide perovskite solar cells: degradation and stability. Energy Environ. Sci. *9*, 323–356.

12. Boyd, C.C., Cheacharoen, R., Leijtens, T., and McGehee, M.D. (2019). Understanding degradation mechanisms and improving stability of perovskite photovoltaics. Chem. Rev. *119*, 3418–3451.

13. Cheacharoen, R., Boyd, C.C., Burkhard, G.F., Leijtens, T., Raiford, J.A., Bush, K.A., Bent, S.F., and McGehee, M.D. (2018). Encapsulating perovskite solar cells to withstand damp heat and thermal cycling. Sustain. Energy Fuels *2*, 2398–2406.

14. Cheacharoen, R., Rolston, N., Harwood, D., Bush, K.A., Dauskardt, R.H., and McGehee, M.D. (2018). Design and understanding of encapsulated perovskite solar cells to withstand temperature cycling. Energy Environ. Sci. *11*, 144–150.

15. Islam, M.B., Yanagida, M., Shirai, Y., Nabetani, Y., and Miyano, K. (2019). Highly stable semi-transparent MAPbI3 perovskite solar cells with operational output for 4000 h. Sol. Energy Mater. Sol. Cells *195*, 323–329.

16. Li, N., Tao, S., Chen, Y., Niu, X., Onwudinanti, C.K., Hu, C., Qiu, Z., Xu, Z., Zheng, G., Wang, L., et al. (2019). Cation and anion immobilization through chemical bonding enhancement with fluorides for stable halide perovskite solar cells. Nat. Energy *4*, 408–415.

17. Ball, J.M., and Petrozza, A. (2016). Defects in perovskite-halides and their effects in solar cells. Nat. Energy *1*, 16149.

18. Kim, J., Lee, S.H., Lee, J.H., and Hong, K.H. (2014). The role of intrinsic defects in methylammonium lead iodide perovskite. J. Phys. Chem. Lett. *5*, 1312–1317.

19. Motta, C., El-Mellouhi, F.E., Kais, S., Tabet, N., Alharbi, F., and Sanvito, S. (2015). Revealing the role of organic cations in hybrid halide perovskite CH3NH3PbI3. Nat. Commun. *6*, 7026.

20. El-Mellouhi, F.E., Marzouk, A., Bentria, E.T., Rashkeev, S.N., Kais, S., and Alharbi, F.H. (2016). Hydrogen bonding and stability of hybrid organic–inorganic perovskites. ChemSusChem *9*, 2648–2655.

21. Egger, D.A., and Kronik, L. (2014). Role of dispersive interactions in determining structural properties of organic–inorganic halide perovskites: insights from first-principles calculations. J. Phys. Chem. Lett. *5*, 2728–2733.

22. Jaffe, A., Lin, Y., and Karunadasa, H.I. (2017). Halide perovskites under pressure: accessing new properties through lattice compression. ACS Energy Lett *2*, 1549–1555.

23. Eames, C., Frost, J.M., Barnes, P.R.F., ÓRegan, B.C., Walsh, A., and Islam, M.S. (2015). Ionic transport in hybrid lead iodide perovskite solar cells. Nat. Commun. *6*, 7497.

24. Azpiroz, J.M., Mosconi, E., Bisquert, J., and De Angelis, F.D. (2015). Defect migration in methylammonium lead iodide and its role in perovskite solar cell operation. Energy Environ. Sci. *8*, 2118–2127.

25. Brivio, F., Caetano, C., and Walsh, A. (2016). Thermodynamic origin of photoinstability in the CH3NH3Pb(I1−xBrx)3 hybrid halide perovskite alloy. J. Phys. Chem. Lett. *7*, 1083–1087.

26. Bischak, C.G., Hetherington, C.L., Wu, H., Aloni, S., Ogletree, D.F., Limmer, D.T., and Ginsberg, N.S. (2017). Origin of reversible photoinduced phase separation in hybrid perovskites. Nano Lett. *17*, 1028–1033.

27. Yoon, S.J., Draguta, S., Manser, J.S., Sharia, O., Schneider, W.F., Kuno, M., and Kamat, P.V. (2016). Tracking iodide and bromide ion segregation in mixed halide lead perovskites during photoirradiation. ACS Energy Lett. *1*, 290–296.

28. Slotcavage, D.J., Karunadasa, H.I., and McGehee, M.D. (2016). Light-induced phase segregation in halide-perovskite absorbers. ACS Energy Lett. *1*, 1199–1205.

29. Tang, X., van den Berg, M., Gu, E., Horneber, A., Matt, G.J., Osvet, A., Meixner, A.J., Zhang, D., and Brabec, C.J. (2018). Local observation of phase segregation in mixed-halide perovskite. Nano Lett. *18*, 2172–2178.

30. Hoke, E.T., Slotcavage, D.J., Dohner, E.R., Bowring, A.R., Karunadasa, H.I., and McGehee, M.D. (2015). Reversible photo-induced trap formation in mixed-halide hybrid perovskites for photovoltaics. Chem. Sci. *6*, 613–617.

31. Draguta, S., Sharia, O., Yoon, S.J., Brennan, M.C., Morozov, Y.V., Manser, J.S., Kamat, P.V., Schneider, W.F., and Kuno, M. (2017). Rationalizing the light-induced phase separation of mixed halide organic–inorganic perovskites. Nat. Commun. *8*, 200.

32. Mei, A., Li, X., Liu, L., Ku, Z., Liu, T., Rong, Y., Xu, M., Hu, M., Chen, J., Yang, Y., et al. (2014). A hole-conductor–free, fully printable mesoscopic perovskite solar cell with high stability. Science *345*, 295–298.

33. Grancini, G., Roldán-Carmona, C., Zimmermann, I., Mosconi, E., Lee, X., Martineau, D., Narbey, S., Oswald, F., De Angelis, F., Graetzel, M., and Nazeeruddin, M.K. (2017). One-year stable perovskite solar cells by 2D/3D interface engineering. Nat. Commun. *8*, 15684.

34. Conings, B., Drijkoningen, J., Gauquelin, N., Babayigit, A., D'Haen, J., D'Olieslaeger, L., Ethirajan, A., Verbeeck, J., Manca, J., Mosconi, E., et al. (2015). Intrinsic thermal instability of methylammonium lead trihalide perovskite. Adv. Energy Mater. *5*, 1500477.

35. Zhou, N., Shen, Y., Zhang, Y., Xu, Z., Zheng, G., Li, L., Chen, Q., and Zhou, H. (2017). CsI Pre-intercalation in the inorganic framework for efficient and stable FA1−xCsxPbI3 (Cl) perovskite solar cells. Small *13*, 1700484.

36. Turren-Cruz, S.H., Hagfeldt, A., and Saliba, M. (2018). Methylammonium-free, high-performance, and stable perovskite solar cells on a planar architecture. Science *362*, 449–453.

37. Chen, Y., Yang, Z., Jia, X., Wu, Y., Yuan, N., Ding, J., Zhang, W.H., and Liu, S. (2019). Thermally stable methylammonium-free inverted perovskite solar cells with Zn2+ doped CuGaO2 as efficient mesoporous hole-transporting layer. Nano Energy *61*, 148–157.

38. Bush, K.A., Palmstrom, A.F., Zhengshan, J.Y., Boccard, M., Cheacharoen, R., Mailoa, J.P., McMeekin, D.P., Hoye, R.L.Z., Bailie, C.D., Leijtens, T., et al. (2017). 23.6%-efficient monolithic perovskite/silicon tandem solar cells with improved stability. Nat. Energy *2*, 17009.

39. Wang, Z., McMeekin, D.P., Sakai, N., van Reenen, S., Wojciechowski, K., Patel, J.B., Johnston, M.B., and Snaith, H.J. (2017). Efficient and air-stable mixed-cation lead mixed-halide perovskite solar cells with n-doped organic electron extraction layers. Adv. Mater. *29*, 1604186.

40. Lee, J.-W., Kim, D.-H., Kim, H.-S., Seo, S.-W., Cho, S.M., and Park, N.-G. (2015). Formamidinium and cesium hybridization for photo- and moisture-stable perovskite solar cell. Adv. Energy Mater. *5*, 1501310.

41. Gao, X.X., Luo, W., Zhang, Y., Hu, R., Zhang, B., Züttel, A., Feng, Y., and Nazeeruddin, M.K. (2020). Stable and high-efficiency methylammonium-free perovskite solar cells. Adv. Mater. *32*, e1905502.

42. Schelhas, L.T., Li, Z., Christians, J.A., Goyal, A., Kairys, P., Harvey, S.P., Kim, D.H., Stone, K.H., Luther, J.M., Zhu, K., et al. (2019). Insights into operational stability and processing of halide perovskite active layers. Energy Environ. Sci. *12*, 1341–1348.

43. Bi, D., Li, X., Milić, J.V., Kubicki, D.J., Pellet, N., Luo, J., LaGrange, T., Mettraux, P., Emsley, L., Zakeeruddin, S.M., and Grätzel, M. (2018). Multifunctional molecular modulators for perovskite solar cells with over 20% efficiency and high operational stability. Nat. Commun. *9*, 4482.

44. Malinauskas, T., Tomkute-Luksiene, D.T., Sens, R., Daskeviciene, M., Send, R., Wonneberger, H., Jankauskas, V., Bruder, I., and Getautis, V. (2015). Enhancing thermal stability and lifetime of solid-state dye-sensitized solar cells via molecular engineering of the hole-transporting material spiro-OMeTAD. ACS Appl. Mater. Interfaces *7*, 11107–11116.

45. Niu, X., Li, N., Zhu, C., Liu, L., Zhao, Y., Ge, Y., Chen, Y., Xu, Z., Lu, Y., Sui, M., et al. (2019). Temporal and spatial pinhole constraints in small-molecule hole transport layers for stable and efficient perovskite photovoltaics. J. Mater. Chem. A *7*, 7338–7346.

46. Li, Z., Xiao, C., Yang, Y., Harvey, S.P., Kim, D.H., Christians, J.A., Yang, M., Schulz, P., Nanayakkara, S.U., Jiang, C.-S., et al. (2017). Extrinsic ion migration in perovskite solar cells. Energy Environ. Sci. *10*, 1234–1242.

47. Domanski, K., Correa-Baena, J.P., Mine, N., Nazeeruddin, M.K., Abate, A., Saliba, M., Tress, W., Hagfeldt, A., and Grätzel, M. (2016). Not all that glitters is gold-metal migration-induced degradation in perovskite solar cells. ACS Nano *10*, 6306–6314.

48. Eze, V.O., Lei, B., and Mori, T. (2016). Air-assisted flow and two-step spin-coating for highly efficient CH3NH3PbI3 perovskite solar cells. Jpn. J. Appl. Phys. *55*, 02BF08.

49. Chen, Q., Zhou, H., Song, T.B., Luo, S., Hong, Z., Duan, H.S., Dou, L., Liu, Y., and Yang, Y. (2014). Controllable self-induced passivation of hybrid lead iodide perovskites toward high performance solar cells. Nano Lett. *14*, 4158–4163.

50. Park, B.W., Kedem, N., Kulbak, M., Lee, D.Y., Yang, W.S., Jeon, N.J., Seo, J., Kim, G., Kim, K.J., Shin, T.J., et al. (2018). Understanding how excess lead iodide precursor improves halide perovskite solar cell performance. Nat. Commun. *9*, 3301.

51. Jiang, Q., Chu, Z., Wang, P., Yang, X., Liu, H., Wang, Y., Yin, Z., Wu, J., Zhang, X., and You, J. (2017). Planar-structure perovskite solar cells

with efficiency beyond 21%. Adv. Mater. *29*, 1703852.

52. Futscher, M.H., Lee, J.M., McGovern, L., Muscarella, L.A., Wang, T., Haider, M.I., Fakharuddin, A., Schmidt-Mende, L., and Ehrler, B. (2019). Quantification of ion migration in CH3NH3PbI3 perovskite solar cells by transient capacitance measurements. Mater. Horiz. *6*, 1497–1503.

53. Kim, G.Y., Senocrate, A., Yang, T.Y., Gregori, G., Grätzel, M., and Maier, J. (2018). Large tunable photoeffect on ion conduction in halide perovskites and implications for photodecomposition. Nat. Mater. *17*, 445–449.

54. Balluffi, R.W., Allen, S.M., and Carter, W.C. (2005). Kinetics of Materials (John Wiley & Sons).

55. Tao, S., Schmidt, I., Brocks, G., Jiang, J., Tranca, I., Meerholz, K., and Olthof, S. (2019). Absolute energy level positions in tin- and lead-based halide perovskites. Nat. Commun. *10*, 2560.

56. Yi, C., Luo, J., Meloni, S., Boziki, A., Ashari-Astani, N., Grätzel, C., Zakeeruddin, S.M., Röthlisberger, U., and Grätzel, M. (2016). Entropic stabilization of mixed A-cation ABX3 metal halide perovskites for high performance perovskite solar cells. Energy Environ. Sci. *9*, 656–662.

57. Johnston, M.B., and Herz, L.M. (2016). Hybrid perovskites for photovoltaics: charge-carrier recombination, diffusion, and radiative efficiencies. Acc. Chem. Res. *49*, 146–154.

58. Davies, C.L., Filip, M.R., Patel, J.B., Crothers, T.W., Verdi, C., Wright, A.D., Milot, R.L., Giustino, F., Johnston, M.B., and Herz, L.M. (2018). Bimolecular recombination in methylammonium lead triiodide perovskite is an inverse absorption process. Nat. Commun. *9*, 293.

59. Lin, Y., Chen, B., Fang, Y., Zhao, J., Bao, C., Yu, Z., Deng, Y., Rudd, P.N., Yan, Y., Yuan, Y., and Huang, J. (2018). Excess charge-carrier induced instability of hybrid perovskites. Nat. Commun. *9*, 4981.

60. Quitsch, W.A., deQuilettes, D.W., Pfingsten, O., Schmitz, A., Ognjanovic, S., Jariwala, S., Koch, S., Winterer, M., Ginger, D.S., and Bacher, G. (2018). The role of excitation energy in photobrightening and photodegradation of halide perovskite thin films. J. Phys. Chem. Lett. *9*, 2062–2069.

61. Vogt, S. (2003). MAPS: a set of software tools for analysis and visualization of 3D X-ray fluorescence data sets. J. Phys. IV France *104*, 635–638.

62. Correa-Baena, J.P., Luo, Y., Brenner, T.M., Snaider, J., Sun, S., Li, X., Jensen, M.A., Hartono, N.T.P., Nienhaus, L., Wieghold, S., et al. (2019). Homogenized halides and alkali cation segregation in alloyed organic-inorganic perovskites. Science *363*, 627–631.

63. Dalpian, G.M., Zhao, X.-G., Kazmerski, L., and Zunger, A. (2019). Formation and composition-dependent properties of alloys of cubic halide perovskites. Chem. Mater. *31*, 2497–2506.

64. Perdew, J.P., Burke, K., and Ernzerhof, M. (1996). Generalized gradient approximation made simple. Phys. Rev. Lett. *77*, 3865–3868.

65. Blöchl, P.E. (1994). Projector augmented-wave method. Phys. Rev. B Condens. Matter. *50*, 17953–17979.

66. Kresse, G., and Furthmüller, J. (1996). Efficient iterative schemes for ab initio total-energy calculations using a plane-wave basis set. Phys. Rev. B Condens. Matter. *54*, 11169–11186.